$^3H(\alpha,\gamma)^7Li$ reaction at low energies

C. R. Brune, R. W. Kavanagh, and C. Rolfs*
W. K. Kellogg Radiation Laboratory, 106-38,
California Institute of Technology, Pasadena, California 91125
(Received 15 June 1994)

The absolute cross section of the $^3H(\alpha,\gamma)^7Li$ reaction has been measured for $50 \leq E_{c.m.} \leq 1200$ keV. Specially prepared ^3H targets were bombarded with an α^+ beam, and γ rays were detected using an 85% high-purity germanium detector. Total S factors and the branching ratios for radiative capture to the two final bound states are reported for the entire energy range. Angular distributions of the capture γ rays were measured for nine energies in the range $115 \leq E_{c.m.} \leq 1200$ keV. Legendre coefficients extracted from fits to the angular distributions are also reported. The energy dependence of the measured S factors is found to be in agreement with existing theoretical calculations. The new results are used to calculate the thermonuclear reaction rate for temperatures below 10 GK, required for computing the ^7Li abundance in primordial nucleosynthesis.

PACS number(s): 25.55.−e, 23.20.En, 27.20.+n, 98.80.Ft

I. INTRODUCTION

The standard big-bang model of the universe is very successful in accounting for the observed abundances (relative to ^1H) of ^2H, ^3He, ^4He, and ^7Li [1–4]. The calculated abundances agree with observations only for baryon densities significantly lower than the critical density, in the range $0.01 \lesssim \Omega_B \lesssim 0.1$. In addition, primordial-nucleosynthesis calculations provide some stringent tests of several of the assumptions underlying the standard big-bang model. Important input data include the known particles (e.g., three neutrino species), nuclear reaction rates, and the neutron lifetime (used to determine the rates for weak $n \leftrightarrow p$ processes).

The two-body thermonuclear reaction rate $N_A\langle\sigma v\rangle$ used in astrophysical calculations is calculated from the cross section σ using

$$N_A\langle\sigma v\rangle = \left(\frac{8}{\pi\mu}\right)^{1/2} \frac{N_A}{(kT)^{3/2}} \int_0^\infty E\,\sigma(E) \times \exp\left(-\frac{E}{kT}\right) dE\,, \quad (1)$$

where N_A is Avogadro's number, μ is the reduced mass in the entrance channel, k is Boltzmann's constant, T is temperature, and E is the center-of-mass energy. The uncertainties in the abundance calculations arising from nuclear-data input have been studied in detail by Krauss and Romanelli [1] and Smith, Kawano, and Malaney [4]. Reference [4] identifies 12 reactions which significantly affect light-element production. Of the 12, the $^3H(\alpha,\gamma)^7Li$ reaction is by far the most uncertain; the authors estimated a 2σ uncertainty of up to 55% in the cross section.

The $^3H(\alpha,\gamma)^7Li$ reaction ($Q = 2467.9$ keV [5]) proceeds by γ emission to the two bound states: the $\frac{3}{2}^-$ ground state (γ_0) or the $\frac{1}{2}^-$ first excited state (γ_1). The first excited state decays by γ emission (γ_2) to the ground state. The (α,γ) cross section is expected to be nonresonant for $E < 2100$ keV, since there is no energy level between the first excited state and the $\frac{7}{2}^-$ state at an excitation energy of 4630 keV. At low energies, the reaction cross section is conveniently parametrized in terms of the S factor $S(E)$, defined by

$$\sigma(E) = \frac{S(E)}{E} \exp\left(-\sqrt{\frac{E_G}{E}}\right), \quad (2)$$

where E is the center-of-mass energy (hereafter, energies without a subscript label refer to the c.m. system), and E_G is the Gamow energy ($E_G = 6735.0$ keV for $^3H + \alpha$). The S factor for a nonresonant reaction such as $^3H(\alpha,\gamma)^7Li$ is expected to be a slowly varying function of energy. The cross sections σ_i for producing γ_i are then determined by S (the S factor summed over both transitions) and the branching ratio $R = \sigma_1/\sigma_0$.

It has been shown [6] that standard big-bang calculations of the ^7Li abundance are sensitive to the $^3H(\alpha,\gamma)^7Li$ reaction rate for $0.1 \lesssim T_9 \lesssim 0.6$, where T_9 is the temperature in GK. These temperatures correspond to effective energies [i.e., most important energies in Eq. (1)] in the range $50 \lesssim E_0 \lesssim 165$ keV.

Previous direct measurements have been made by Griffiths *et al.* [7], Schröder *et al.* [8], and Burzynski *et al.* [9]. The measurements of S are in reasonable agreement over the range of their mutual overlap, if the respective systematic errors (quoted between 14 and 25%) are taken into account. However, only the experiment of Schröder *et al.* reaches the low energies needed to determine big-bang ^7Li production. The measurements of Griffiths *et al.* and Burzynski *et al.* are consistent with a constant value, $S \approx 0.064$ keV b. The data of Schröder

*Present Address: Ruhr-Universität Bochum, Experimentalphysik III, Postfach 102148, D-4630 Bochum 1, Germany.

et al. show a significant increase with decreasing energy, leading to $S(0) = 0.13 - 0.16$ keV b, depending upon the extrapolation used. The measured values of the branching ratio are consistent with a constant value, but they are in poor agreement: Griffiths *et al.* find $R \approx 0.40$, Schröder *et al.* find $R = 0.32 \pm 0.01$, and Burzynski *et al.* find $R \approx 0.51$. Griffiths *et al.* reported limited angular-distribution measurements at $E = 241$ and 567 keV.

A disturbing development is the new measurement by Feldman *et al.* [10] of the ^{3}H(p,γ) cross section used by Griffiths *et al.* and Schröder *et al.* to determine the ^{3}H areal density of their targets. The new data cover $2 \leq E_p \leq 15$ MeV, and are $\approx 30\%$ lower than the cross sections found by Perry and Bame [11] (who quoted an uncertainty of 7%). The ramifications of this measurement for the absolute normalization of the Griffiths *et al.* and Schröder *et al.* S factors are not clear, as the new measurement has not been independently confirmed, and it only covers higher energies than used in the (α,γ) experiments. A possible systematic error in the NaI scintillator efficiency used by Perry and Bame is discussed by Griffiths *et al.*

Indirect measurements of the energy dependence of the S factor using the Coulomb breakup of ^{7}Li have been reported by Utsunomiya *et al.* [12]. Absolute cross sections were not determined; they normalized to $S(500\text{ keV}) = 0.060$ keV b. The measured energy dependence is in agreement with that of Schröder *et al.*, but the low-energy uncertainties are very large. Further breakup measurements were reported by Gazes *et al.* [13], but no attempt was made to extract ^{3}H(α,γ) cross sections.

The existing theoretical calculations of the energy dependence of $S(E)$ [14–19] predict an increasing $S(E)$ at low energies. None of the calculations predicts as large an increase in the low-energy S factor as found by Schröder *et al.* or Utsunomiya *et al.* Calculations of the branching ratio [15,18–20] predict R to be nearly energy independent, with values in the range 0.41–0.47.

We report new measurements of the ^{3}H$(\alpha,\gamma)^7$Li reaction for $50 \leq E \leq 1200$ keV. Angular distributions were measured for nine energies in the range $115 \leq E \leq 1200$ keV. Previous experiments have relied on various assumptions about the angular distribution for extracting the total cross section. The new data are used to calculate the thermonuclear reaction rate for temperatures less than 10 GK. Additional details of the experiment and the data analysis are available in Ref. [6].

II. EXPERIMENTAL APPARATUS AND PROCEDURES

The experiment was carried out by bombarding a Ti-^{3}H target with an α^+ beam, and detecting the γ rays with a large-volume Ge detector. Systematic errors in the absolute cross section are considerably reduced compared to previous experiments, primarily due to our more accurate determination of the ^{3}H areal density, and reduced uncertainties in γ-ray spectroscopy.

A. Beam

The proton, deuteron, and α^+ beams used in this experiment were supplied by the Caltech 3-MV Pelletron Tandem Accelerator. The beam energy was defined by a 90° analyzer magnet and NMR magnetometer. The energy calibration ($\pm 0.1\%$) was established using the (483.91 ± 0.10)-keV resonance [21] in ^{19}F$(p,\alpha\gamma)$, the (991.86 ± 0.03)-keV resonance [22] in ^{27}Al(p,γ), the (606.0 ± 0.5)-keV resonance [23] in ^{11}B(α,n), and the (1530.03 ± 0.15)-keV resonance [24] in ^{24}Mg(α,γ). This energy calibration was used for the measurements described in Sec. II B; the energy scale for the ^{3}H(α,γ) measurements was deduced from the energy of the capture γ rays. The number of incident particles was determined by beam-current integration. The calibration of the integrator was tested with current sources over the range 20 nA–30 μA, and found to be accurate within 0.5%. The effect of leakage current through the H_2O-cooling lines used during the ^{3}H(α,γ) experiments was measured to be $< 0.5\%$.

B. ^{3}H targets

The preparation and characterization of the Ti-^{3}H targets has been described previously [25]. Briefly, Ti was evaporated onto 31.7-mm-diameter, 0.81-mm-thickness Cu substrates; the substrates were then heated in an atmosphere of $^3H_2$ gas to induce the formation of Ti-^{3}H. The substrates were maintained in high vacuum during the time between Ti evaporation and tritide formation, minimizing Ti contamination and maximizing the attainable ^{3}H:Ti ratio.

The ^{3}H and Ti areal densities were determined using the ^{3}H(d,α) and Ti(α,α) reactions, respectively. The charged particles were detected at $\theta_{\text{lab}} = 165°$ with a silicon surface-barrier detector collimated to have a solid angle of 1.194 ± 0.018 msr. The beam, collimated to a 1.6-mm diameter, was incident normal to the target. The target was biased at +300 V in order to ensure accurate beam-current integration by preventing secondary electron emission, and the collimator was followed by a −400 V suppression ring. A pulser peak was inserted above the spectrum to monitor dead-time corrections (typically less than 5%).

The beam-current integration and detector solid angle were checked by measuring the Cu(p,p) yield from a thick Cu substrate for $2000 \leq E_p \leq 2600$ keV, where the cross section is known to follow the Rutherford formula [26], and where the proton-stopping power [27] is known to 1%. The expected height of the plateau at its edge can be calculated from the differential cross section and stopping power as described by Sargood [28]. The measured values were in excellent agreement with calculated values over the entire range; for example, the measured and calculated values at $E_p = 2200$ keV were $(9.22 \pm 0.17) \times 10^4$ and $(9.03 \pm 0.09) \times 10^4$ protons keV^{-1} μC^{-1} sr^{-1}, respectively.

Ti areal densities were determined by elastic α scattering for $1500 \leq E_\alpha \leq 2250$ keV, where the cross section

is given by the Rutherford formula. The uniformity of the Ti layers was excellent; the areal density was found to decrease slowly with distance from the center of the target (6% lower at 12 mm from center), consistent with the substrate–Ti-source evaporation geometry.

The ^3H areal densities of the targets were determined using the $^3H(d,\alpha)$ reaction. The total cross section and center-of-mass Legendre coefficients for this reaction were taken from the evaluation of Drosg and Schwerer [29]; the uncertainty is estimated to be 1.5% for $E_d < 400$ keV, increasing to 4% for higher energies.

The majority of the targets were tested over the range $250 \leq E_d \leq 700$ keV. The observed spectra were consistent with the ^3H being uniformly distributed in the Ti, with no ^3H in the target backing. Examples of $Ti(\alpha,\alpha)$ and $^3H(d,\alpha)$ spectra obtained with target 1 are shown in Figs. 4 and 6 of Ref. [25]. The (d,α) excitation functions obtained from the four targets used in this work are shown in Fig. 1, along with fits to the energy dependence of Drosg and Schwerer. In all cases the energy dependence of the α yield (including small corrections for energy loss) was consistent with the evaluated cross sections. The measured Ti and ^3H areal densities for each target are given in Table I. The ^3H:Ti ratio was found to be constant within 3% over the surface of the targets.

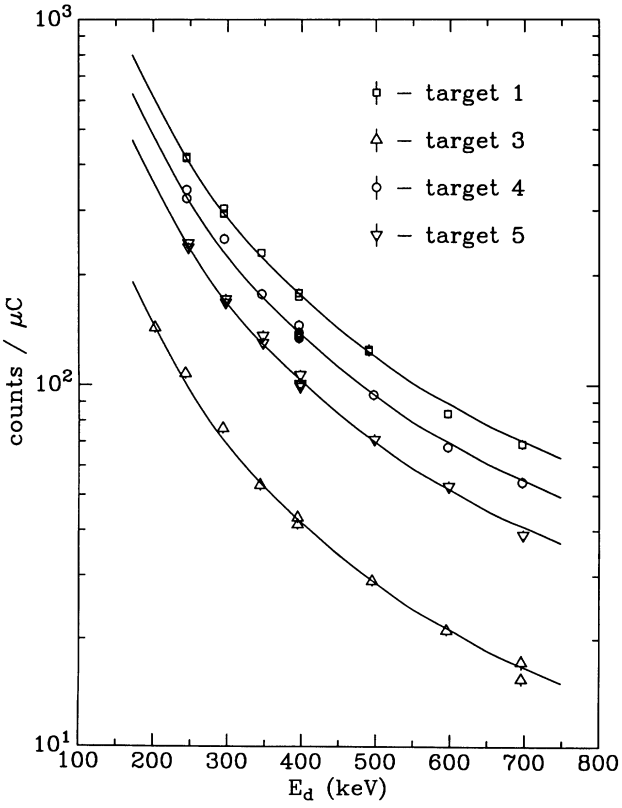

FIG. 1. $^3H(d,\alpha)$ excitation functions obtained from targets 1 and 3–5. The solid curves are the recommended cross sections [29], normalized to the data.

C. Experimental configurations

The $^3H(\alpha,\gamma)$ reaction was measured using three different experimental configurations, labeled geometries A, B, and C. For geometry A, the target was perpendicular to the beam, and the γ-ray detector was positioned at 0°, with the front face of the Ge detector 2.1 cm from the Ti-^3H layer. This setup is depicted in Fig. 2. Geometry B was identical to A, except that the detector was much farther from the target (11.6 cm from source to Ge front face). For geometry C, used for the angular-distribution measurements, the target was at 45° with respect to the beam, and the detector was placed on a rotating table oriented at five angular positions: 0°, −45°, −90°, +90°, and +135°. The distance from the source to the Ge front face was 10.1 cm. The uncertainty in the angular positions is estimated to be ±2°.

In each case the targets were sealed against a circular knife edge at the end of the target chamber. The back sides of the targets were cooled with flowing chilled water in order to dissipate the beam power. For geometries A and B, the beam was collimated by a 12.7-mm-diameter aperture 62–75 cm upstream from the target. For geometry C a rectangular collimator (4.0 mm horizontal × 15.9 mm vertical) 53 cm upstream from the target was used. In order to bombard the target uniformly and reproducibly, the focused beam was rastered over the area of the collimator by magnetic steerers. A −400 V suppression ring between the target and the collimator ensured accurate current integration.

The beamline and target vacuum were maintained at $\approx 3 \times 10^{-7}$ torr during the experiments. An unexplained buildup of $\approx 5 \times 10^{17}$ atoms/cm^2 of carbon occurred during the experiments with target 1, in spite of the use of a liquid-N_2-temperature cold trap near the target. For the subsequent measurements, the cold trap was removed, and the beamline parts were thoroughly recleaned; $< 1.5 \times 10^{16}$ atoms/cm^2 of carbon was found after these measurements, as described below in Sec. II E.

D. γ-ray detection

Gamma rays were detected using an 85% relative-efficiency high-purity Ge detector, shielded by 5–10 cm of Pb. The signals were processed by a spectroscopy amplifier and stored in a 4096-channel analyzer. The spectra were transferred to a computer for off-line analysis. The energy resolution of the detector was typically 2.1 keV at $E_\gamma = 1332$ keV.

The photopeak efficiency ε was determined for the needed range of γ-ray energies in each geometry (including each angle for the angular-distribution setup) using the following sources: ^{152}Eu, ^{56}Co, and ^{24}Na. The absolute strength of the ^{152}Eu source was determined by comparison with a NBS source No. 4275, the strength of the ^{24}Na was determined using the coincident-sum peak, and the strength of the ^{56}Co source was determined by comparison with the other sources.

Coincident-summing corrections to the radioactive-source data and also the $^3H(\alpha,\gamma)$ data are very impor-

TABLE I. The ^{3}H and Ti areal densities determined for each target. The ^{3}H areal densities are given before and after the α^+ bombardments (consisting of total incident charge Q). Also given are the number of data points N and the χ^2 (using only statistical errors) for the initial fits to the ^{3}H(d,α) cross section. The numbers given in parentheses with the ^{3}H areal densities are the statistical errors in the least significant digit, scaled by $\sqrt{\frac{\chi^2}{N-1}}$.

Target	Ti (before) (10^{17}/cm^2)	^{3}H (before) (10^{17}/cm^2)	N	χ^2	Q (C)	^{3}H (after) (10^{17}/cm^2)
1	2.96	5.52(4)	13	13.1	1.573	5.36(6)
3	4.67	1.32(2)	10	17.4	1.036	1.32(4)
4	2.86	4.33(4)	14	17.5	5.905	2.55(11)[a]
5	1.90	3.23(3)	13	13.2	0.690	2.97(3)

[a]Determined from decrease in yield seen in repeated measurements at E_α = 1000 keV.

tant, especially for geometry A. Care was taken during the γ-ray calibrations to use the same Pb-shielding arrangement as during the ^{3}H(α,γ) measurements, so that the total efficiency, which is needed for making the summing corrections, was the same.

The total efficiency η was determined by measuring the photofraction ϕ defined to be the ratio of photopeak efficiency to total efficiency. The total efficiency includes events where γ rays interact in the Ge crystal, but do not deposit their full energy, as well as events in which radiation is scattered into the detector by material in the vicinity of the target and detector (possible "scattering" mechanisms include the Compton effect, pair production, 511-keV radiation from the annihilation of positrons, bremsstrahlung, and x-ray fluorescence). It is clear that the presence of the target chamber and Pb shielding increases the total efficiency relative to a bare detector.

The photofraction was measured as a function of E_γ using various sources. An ideal source would emit isotropic, monoenergetic γ rays, with no other radiation. In practice, such sources are rare, so use has been made of several "nonideal" sources, with appropriate corrections. Due to the presence of noise in the detector electronics, a low-energy threshold (13–100 keV, depending on gain settings) was required in the detector spectrum. The extrapolation of the spectra to zero pulse height involved a correction of 3–9 %. The spectra were corrected for background from the room as well as source impurities and noncoincident γ rays from the source. Most of the measurements were performed in geometry A, where coincident-summing effects were most important.

Measurements were made using ^{57}Co (E_γ = 122 keV), ^{51}Cr (E_γ = 320 keV), ^{198}Au (E_γ = 412 keV), the ^{7}Li(p,p_1) reaction at E_p = 1200 keV (E_γ = 478 keV), ^{137}Cs (E_γ = 662 keV), ^{54}Mn (E_γ = 835 keV), ^{60}Co (E_γ = 1172 and 1332 keV), the ^{12}C$(p,\gamma)^{13}$N reaction at E_p = 461 keV (E_γ = 2370 keV), ^{24}Na (E_γ = 2754 keV), and the ^{19}F$(p,\alpha\gamma)$ reaction at E_p = 340 keV (E_γ = 6130 keV). The results obtained for geometry A are shown in Fig. 3. The photofractions used for geometries B and C were based upon more limited measurements and Monte Carlo calculations (described below).

The mean reaction energy for the ^{3}H(α,γ) measurements was determined from the centroid of the γ_0 peak and reaction kinematics (the details of the analysis are described in Sec. III). An accurate determination of the detector's energy calibration is a crucial ingredient in this determination, particularly in the range 2500 $\leq E_\gamma \leq$ 2700 keV, corresponding to the lowest α energies where the energy dependence of the cross section is greatest.

The energy calibration was based upon the accurately known ^{24}Na lines at E_γ = 1368.633(6) and 2754.030(14) keV [30]. The calibrations were performed

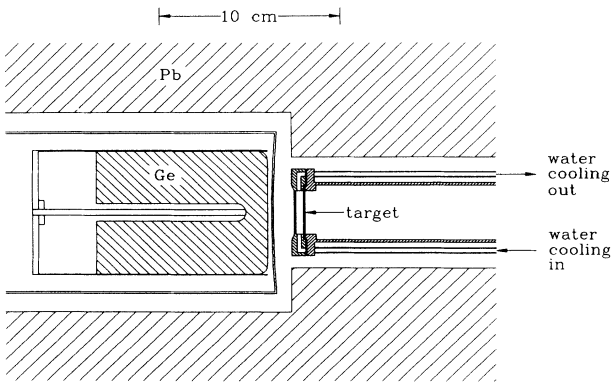

FIG. 2. The details of geometry A, showing the target chamber and the position of the high-impurity Ge γ-ray detector.

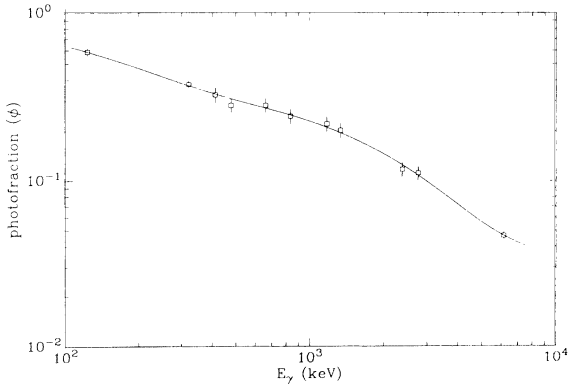

FIG. 3. The photofraction ϕ for geometry A. The squares are the experimental points, and the solid curve is the empirical fit used in subsequent analysis.

daily during the ^{3}H(α,γ) experiments. The calibration was taken to be a linear fit to the centroids of the two ^{24}Na lines. The energy calibration in the range $2500 \leq E_\gamma \leq 2700$ is assigned a 0.3-keV systematic uncertainty.

E. Procedure

After each target was made, its ^{3}H and Ti areal densities were determined as described in Sec. II B. The target was then installed in the target chamber for (α,γ) measurements. The incident beam energies were chosen so that the 2614-keV background line would not interfere with the capture γ rays. The most extensive measurements were performed using target 1; targets 3 and 5 were primarily used to test the reproducibility of the absolute cross section and to make additional measurements at low energies. Many repeated measurements at $E_\alpha = 1000$ keV were performed to test for possible target deterioration over time. Measurements using targets 1, 3, and 5 were made in geometries A and B for each. The measurements using target 4 were made in geometry C.

The ^{3}H areal-density determinations using ^{3}H(d,α) were repeated after the (α,γ) measurements for targets 1, 3, and 5. The areal density of target 4 was observed to deteriorate by $\approx 40\%$ over the course of the experiment, as evidenced by the decrease in yield at $E_\alpha = 1000$ keV. The before-and-after results are shown in Table I.

During the experiments with target 1, the capture γ rays for the repeated $E_\alpha = 1000$ keV runs were at a slightly lower energy in the later runs compared to the earlier runs. It was suspected that this energy shift was due a buildup of carbon on the target. This speculation was confirmed by measuring γ rays from the ^{12}C(p,γ) resonance at $E_p = 461$ keV, where it was found that $\approx 5 \times 10^{17}$ atoms/cm^2 of carbon were deposited. Subsequent measurements of the ^{13}C(α,n) resonance at $E_\alpha = 1053$ keV [31] indicated that the carbon layer was nonuniformly distributed over the target: the 1σ energy spread of the beam emerging from the carbon was deduced to be ≈ 8 keV, well in excess of the value expected for a uniform layer of this thickness.

III. DATA ANALYSIS

A. Kinematics

The energy of the capture γ rays as a function of the α-particle lab energy E_α and the lab angle θ_L is given by

$$E_\gamma(E_\alpha,\cos\theta_L) = \frac{Q(M_T+M_\alpha+M_7)+2M_T E_\alpha}{2[M_T+M_\alpha+E_\alpha-\cos\theta_L\sqrt{E_\alpha(E_\alpha+2M_\alpha)}]}\,, \tag{3}$$

where M_T, M_α, and M_7 are the rest masses (in energy units) of the ^{3}H, α, and ^{7}Li final state. The ^{7}Li nucleus may be left either in its ground or first excited state ($E_x = 477.61$ keV [32]). The masses and Q value, $Q = M_T + M_\alpha - M_7$, are taken from a recent evaluation [5]. The ground-state Q value used (2467.9 ± 0.7 keV) is significant because it is used in the extraction of the effective reaction energy from the observed γ_0 energy. The error in Q leads to a ± 0.7-keV systematic uncertainty in the center-of-mass energy.

The differential cross section in the center-of-mass system is given by

$$\frac{d\sigma_i}{d\Omega_{\rm c.m.}} = \frac{\sigma_i}{4\pi} W^i_{\rm c.m.}(\theta_{\rm c.m.})\,, \tag{4}$$

where σ_i is the total cross section for producing γ_i. The normalized angular distribution, $W^i_{\rm c.m.}$, is expanded in Legendre polynomials

$$W^i_{\rm c.m.} = 1 + \sum_{\ell=1}^{\infty} a^i_\ell P_\ell(cos\theta_{\rm c.m.})\,. \tag{5}$$

The decay of the $\frac{1}{2}^-$ first excited state is isotropic and uncorrelated with the feeding γ ray; hence the a^2_ℓ should be identically zero. The differential cross section in the lab system is

$$\frac{d\sigma_i}{d\Omega_L} = \frac{\sigma_i}{4\pi} W^i_L(\theta_L)\,, \tag{6}$$

where the normalized angular distribution in the lab system is calculated from Eq. (5):

$$W^i_L = 1 + 2\beta P_1(\cos\theta_L) + \sum_{\ell=1}^{\infty} a^i_\ell \Big\{ P_\ell(\cos\theta_L) + \frac{\beta}{2\ell+1}[(\ell+1)(\ell+2)P_{\ell+1}(\cos\theta_L) - \ell(\ell-1)P_{\ell-1}(\cos\theta_L)] \Big\}\,, \tag{7}$$

to first order in β. Note that $\beta \leq 0.022$ in this experiment, so this is an excellent approximation.

The lifetime of the first excited state of ^{7}Li ($\tau = 105 \pm 3$ fs [32]) is such that the ion velocity is significantly reduced (on average) before decaying. We use $\beta_{\rm eff} = 0.75\beta$ for this transition, where 0.75 is the Doppler-shift attenuation factor found [33] for this state with similar-velocity ^{7}Li ions stopping in Ni.

B. γ-ray spectra

Examples of the γ-ray spectra obtained are shown in Fig. 4 (at the lowest energy measured), Fig. 5 (at an intermediate energy), and Fig. 6 (at the highest energy). The numbers of counts in the ^{3}H(α,γ) peaks and the peak centroids were extracted using linear least-squares fits to the background on either side of the peaks. In the angular-distribution measurements with $E_\alpha \geq 1500$ keV

and detector angles $-45°$, $-90°$, $+90°$, or $+135°$, the capture γ-ray peaks were Doppler broadened such that the first-escape peak from γ_0 interfered with the γ_1 peak (see, for example, Fig. 6). These cases were treated by extracting the combined number of counts in the γ_0 first-escape and γ_1 peaks, and then subtracting the γ_0 first-escape contribution calculated from the number of counts in the γ_0 peak and the ratio of first-escape peak to photopeak. This ratio was determined for geometry C using the ^{56}Co source and the $0°$ ^{3}H(α,γ) data (where the Doppler broadening was much smaller). An unexpected neutron background was observed for $E_\alpha \lesssim 400$ keV. It was determined that the neutrons originated from the ^{3}H$(^3$H$, 2n)$ reaction, where the ^{3}H projectiles resulted from ^{3}H$(\alpha, ^3$H) elastic scattering. This background made further Pb shielding of the detector or cosmic-ray rejection unimportant.

C. Monte Carlo simulations

Monte Carlo simulations of the γ-ray detector response were used to supplement the information found using radioactive sources. In particular, one can determine the distribution of γ-ray emission angles for detected γ rays using the simulation. This information is important for making finite-detector-size corrections to the angular distributions, and also for extracting the effective reaction energy from the observed energy of the γ_0 transition. This information is not readily attainable experimentally from radioactive sources. The simulations were performed using the ELECTRON GAMMA SHOWER (EGS4) code developed at Stanford [34].

The details of the target chamber, detector, and Pb shielding (as shown, for example, in Fig. 2) were included in the simulation. The simulations reproduced the measured photopeak efficiency ε and photofraction ϕ within 15% over the range $120 \leq E_\gamma \leq 3500$ keV for each geometry. Over the range $2000 \leq E_\gamma \leq 3500$ keV, the agreement was within about 5%.

The angular-distribution attenuation factors [35] were calculated as a function of E_γ from the simulated distribution of γ-ray emission angles. We distinguish between photopeak attenuation factors Q_ℓ^ϵ, which are calculated from events which deposit the full γ-ray energy, and total attenuation factors Q_ℓ^γ, which are calculated from all detected events.

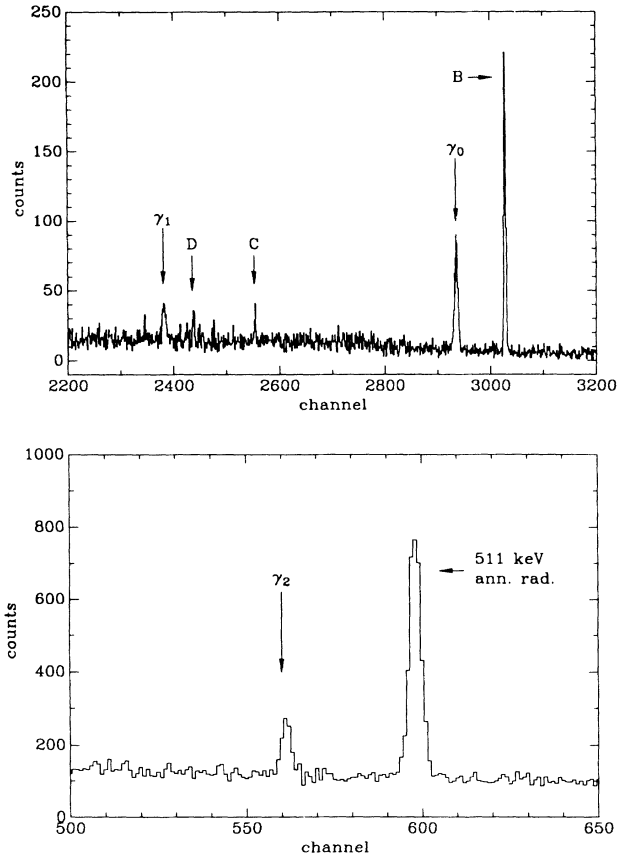

FIG. 4. High-energy (upper panel) and low-energy (lower panel) portions of the spectrum obtained with target 5, geometry A, and $E_\alpha = 140$ keV, showing the γ_0, γ_1, and γ_2 transitions. The peak labeled B is a background line at 2614 keV from ^{208}Tl decay (^{232}Th decay product). Peak C is a background line at 2204 keV from ^{214}Bi decay (^{226}Ra decay product). Peak D is the first-escape peak associated with peak B.

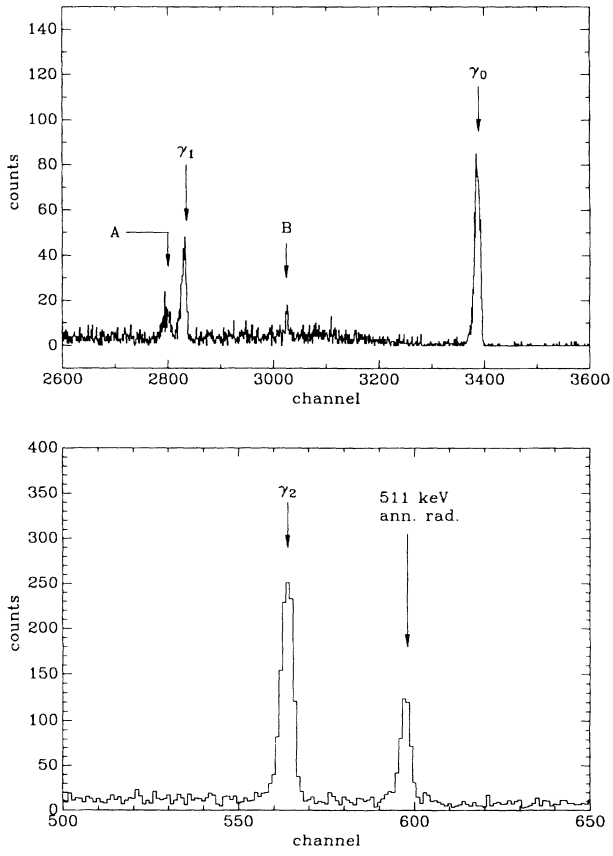

FIG. 5. High-energy (upper panel) and low-energy (lower panel) portions of the spectrum obtained with target 5, geometry A, and $E_\alpha = 1000$ keV, showing the ^{3}H(α,γ) transitions. The peak labeled A is the γ_0 first-escape peak; peak B is a background line at 2614 keV from ^{208}Tl decay (^{232}Th decay product). The energy calibration is the same as for the spectrum shown in Fig. 4.

D. Detector efficiency

The ^{24}Na sources were used to determine the photopeak efficiency at 1368 and 2754 keV, using the coincident-sum peak. The analysis included the angular correlation between the γ rays, the attenuation coefficients, and all coincident-summing effects.

The efficiency results from the ^{56}Co and ^{152}Eu sources were corrected for coincident summing using the technique of Semkow *et al.* [36]. Using decay-scheme information, the full coincidence correction from all possible γ-ray combinations is calculated. The effects of "summing out" (loss of photopeak counts due to coincidentally detected radiation) and "summing in" (increase in photopeak counts of a crossover γ ray due to coincident photopeak detection of the cascade γ rays) are included. The effects of annihilation radiation from coincident β^+ particles are also included. The angular correlation between γ rays is neglected in this calculation, justified on the grounds that in a close geometry, when the coincidence correction is large, the angular correlation is much reduced due to the attenuation coefficients. In a distant geometry, the coincidence correction is small, so an error in the correction due to angular correlation is less significant.

The results for geometry A are shown in Fig. 7. The uncorrected efficiencies show considerable scatter, and are usually lower than the true efficiency. The corrections for geometries B and C were much smaller ($\approx 3\%$), due to greater source distances.

E. Target deterioration

The ^{3}H areal density was observed to deteriorate under α bombardment (see Table I for before-and-after results). Corrections were made assuming that the ^{3}H areal density after cumulative charge Q (measured in μC) is $(nt)_T F_L(Q)$, where $(nt)_T$ is the initial areal density and

$$F_L(Q) = 1 - \int_0^Q \frac{dQ'\, F_s}{[E_\alpha(Q')]^{0.74}\,(nt)_{\rm Ti}} \,. \tag{8}$$

The quantity F_s is a constant, E_α is the incident α energy in keV, and $(nt)_{\rm Ti}$ is the initial Ti areal density in 10^{17} cm^{-2}. The sputtering rate is expected [37] to be proportional to the nuclear stopping power. The nuclear stopping power for α's in Ti [27] is approximately

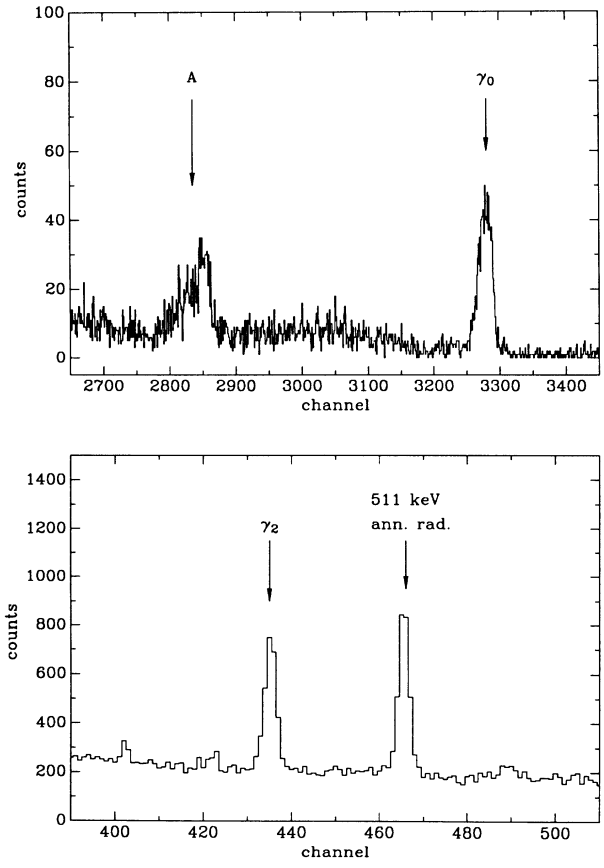

FIG. 6. High-energy (upper panel) and low-energy (lower panel) portions of the spectrum obtained with target 4, geometry C, and $E_\alpha = 2790$ keV, with the detector in the $-90°$ position. The γ_0 transition is cleanly resolved, but the γ_1 transition and the first-escape peak from the γ_0 transition overlap (peak A). The energy calibration is different from the spectra shown in Figs. 4 and 5.

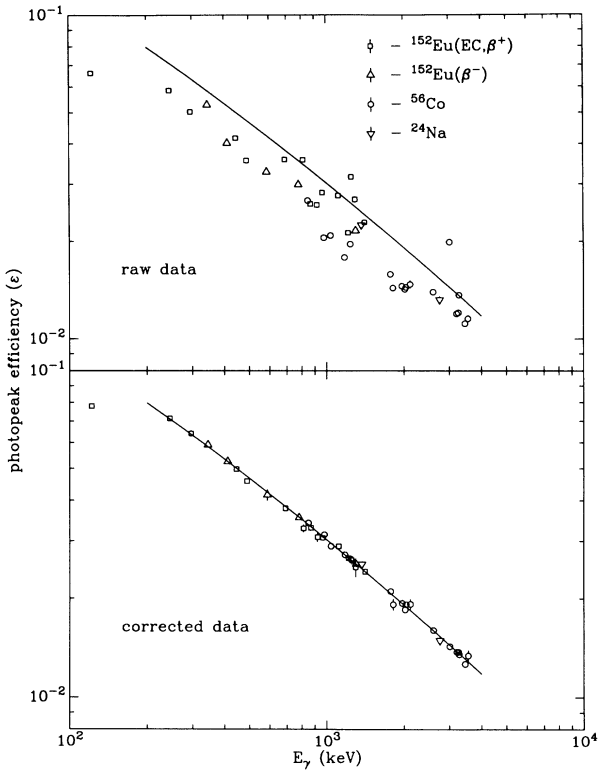

FIG. 7. The photopeak efficiency for geometry A. The upper panel shows the results without correction for coincident summing, while the lower panel shows the results including summing corrections. The solid curve on both panels is the empirical fit to the corrected data for $300 \le E \le 4000$ keV, used in subsequent analysis.

$\propto E_\alpha^{-0.74}$ (over our range of energy), so this dependence is included in Eq. (8). The constant F_s is 4.0×10^{-6} for targets 1, 3, and 5 (geometries A and B) and 1.8×10^{-5} for target 4 (geometry C). These values were found to reproduce the deteriorations observed after the (α,γ) measurements. The error in the correction was assumed to be 40% of the correction, i.e., $\Delta F_L(Q) = 0.4[1 - F_L(Q)]$. From the positions of the centroids and the widths of the γ_0 peaks obtained from target 4, it was determined that the Ti was lost from the target in the same proportion as the ^{3}H. The ^{3}H areal density was also corrected for radioactive decay of the ^{3}H ($< 1\%$).

F. Extraction of cross sections

The effective reaction energy $\bar{E}$ is found from the observed γ_0 centroid $\bar{E}_{\gamma 0}$ by inverting Eq. (3) to find E_α, and then converting the results to the center-of-mass system. In Eq. (3), we use $E_\gamma = \bar{E}_{\gamma 0}$ and $\cos\theta_L = Q_1^\epsilon(\bar{E}_{\gamma 0})\cos\theta_D$, where Q_1^ϵ is the photopeak attenuation factor and θ_D is the angle of the center of the detector with respect to the incident beam. At $E = 50$ keV, the estimated 2% uncertainty in Q_1^ϵ contributes ± 0.2-keV uncertainty to $\bar{E}$.

The observed angular distributions $\overline{W}_L^i(\delta)$, which include the effects of finite detector size, are given by Eq. (7), where $P_\ell(\cos\theta_L)$ is replaced by $Q_\ell^\delta(\bar{E}_{\gamma i})P_\ell(\cos\theta_D)$, and $\delta = \varepsilon$ or η determines whether photopeak or total attenuation factors are to be used. We define ε_i to be the photopeak efficiency evaluated at the observed centroid of γ_i (the energy for γ_1 is calculated from γ_0 and reaction kinematics). The total efficiencies η_i are calculated from ε_i and $\phi(E_{\gamma i})$. The effective efficiencies $\tilde{\varepsilon}_i$, which include coincident-summing corrections, are defined by

$$\tilde{\varepsilon}_0 = \varepsilon_0 + 0.44\varepsilon_1\varepsilon_2 \frac{\overline{W}_L^1(\varepsilon)\overline{W}_L^1(\varepsilon)}{\overline{W}_L^0(\varepsilon)} , \tag{9}$$

$$\tilde{\varepsilon}_1 = \varepsilon_1[1 - \eta_2 \overline{W}_L^2(\eta)] , \tag{10}$$

and

$$\tilde{\varepsilon}_2 = \varepsilon_2[1 - \eta_1 \overline{W}_L^1(\eta)] . \tag{11}$$

The term added to ε_0 includes the effect of coincident photopeak detection of γ_1 and γ_2; the factor 0.44 is the branching ratio σ_1/σ_0 (Sec. IV). The terms subtracted from ε_1 and ε_2 correct for the lost counts due to the coincident detection of the other cascade member.

The number of counts in γ-ray peak i per incident α, Y_i, is related to the experimental cross section at $\bar{E}$, $\sigma_i(\bar{E})$, by

$$Y_i = f(nt)_T F_L(\overline{Q})\sigma_i(\bar{E})\tilde{\varepsilon}_i \, \overline{W}_L^i(\varepsilon) , \tag{12}$$

where f is a deconvolution factor defined below, and $\overline{Q}$ is the cumulative charge up to the halfway point in the run.

If the cross section is known and the target consists of a homogeneous Ti-^{3}H layer, the expected γ_0 yield Y_0^c can be calculated:

$$Y_0^c = (nt)_T \, F_L(\overline{Q}) \, \overline{W}_L^i(\varepsilon) \times \frac{\int_{E_\alpha - \Delta E_\alpha}^{E_\alpha} \sigma_0(E'_\alpha) \, \tilde{\varepsilon}_0[E_{\gamma 0}(E'_\alpha)] \, [\frac{dE_\alpha}{dX}(E'_\alpha)]^{-1} \, dE'_\alpha}{\int_{E_\alpha - \Delta E_\alpha}^{E_\alpha} [\frac{dE_\alpha}{dX}(E'_\alpha)]^{-1} \, dE'_\alpha} , \tag{13}$$

where $\frac{dE_\alpha}{dX}$ is the effective stopping power for α's in Ti-^{3}H and ΔE_α is the energy lost in the target. The quantity $E_{\gamma 0}(E'_\alpha)$ is calculated using Eq. (3) with $\cos\theta_L$ replaced by $Q_1^\epsilon \cos\theta_D$. The energy of the γ_0 centroid can also be calculated:

$$\bar{E}_{\gamma 0}^c = \frac{\int_{E_\alpha - \Delta E_\alpha}^{E_\alpha} E_{\gamma 0}(E'_\alpha) \, \sigma_0(E'_\alpha) \, \tilde{\varepsilon}_0[E_{\gamma 0}(E'_\alpha)] \, [\frac{dE_\alpha}{dX}(E'_\alpha)]^{-1} \, dE'_\alpha}{\int_{E_\alpha - \Delta E_\alpha}^{E_\alpha} \sigma_0(E'_\alpha) \, \tilde{\varepsilon}_0[E_{\gamma 0}(E'_\alpha)] \, [\frac{dE_\alpha}{dX}(E'_\alpha)]^{-1} \, dE'_\alpha} . \tag{14}$$

The calculated γ-ray centroid $\bar{E}_{\gamma 0}^c$ can be converted to an effective reaction energy $\bar{E}^c$ as described in the beginning of this subsection. In order for the calculated yield to be consistent with Eq. (12), the correction factor f must be given by

$$f = \frac{\int_{E_\alpha - \Delta E_\alpha}^{E_\alpha} \sigma_0(E'_\alpha) \, \tilde{\varepsilon}_0[E_{\gamma 0}(E'_\alpha)] \, [\frac{dE_\alpha}{dX}(E'_\alpha)]^{-1} \, dE'_\alpha}{\sigma(\bar{E}^c) \, \tilde{\varepsilon}_0(\bar{E}_{\gamma 0}^c) \int_{E_\alpha - \Delta E_\alpha}^{E_\alpha} [\frac{dE_\alpha}{dX}(E'_\alpha)]^{-1} \, dE'_\alpha} . \tag{15}$$

The energy dependence of σ_0 in Eqs. (14) and (15) is assumed to be given by Eq. (2), with the energy dependence of $S(E)$ taken from Ref. [38]. The attenuation factors used implicitly in Eqs. (14) and (15) are evaluated at the experimental γ_0 centroid $\bar{E}_{\gamma 0}$ in view of the negligible energy dependence of $Q_\ell^\epsilon(E_\gamma)$. The calculation of f was further simplified by using ε_0 in place of $\tilde{\varepsilon}_0$ in Eqs. (14) and (15). This analysis of the correction factor ignores straggling of the beam and the energy dependences of the angular distribution and branching ratio.

For targets 3, 4, and 5, f was calculated using Eqs. (14) and (15), with E_α calculated from the magnetometer calibration. For target 1, the calculation was modified to take into account the energy loss and energy spread due to the nonuniform layer of carbon that was deposited. The carbon-layer thickness was adjusted for each run; the values used were found by interpolating between values inferred from the $\bar{E}_{\gamma 0}$ shifts observed in the repeated $E_\alpha = 1000$ keV runs. The correction factor differs from unity by more than 1% only for the measurements with

$E \lesssim 120$ keV, as it arises primarily from the strong energy dependence of the cross section; it differs from unity by at most 6%. The uncertainty in f is taken to be 40%, i.e., $\Delta f = 0.4|1 - f|$.

1. Angular distributions

The factors $\overline{W}^i_L(\delta)$ used for summing corrections in Eqs. (9), (10), and (11) were calculated by taking a^0_2 and a^1_2 from Ref. [39], setting $a^0_1 = 0.0$, $a^0_3 = 0.05$, $a^1_1 = 0.08$, $a^1_3 = -0.05$, and setting $a^i_{\ell>3}$ to zero. These choices will be justified by the results presented in Sec. IV. For each γ-ray line, $\sigma_i(\bar{E})\overline{W}^i_L(\varepsilon)$ was extracted using Eq. (12). This quantity was then converted to $S_i(\bar{E})\overline{W}^i_L(\varepsilon)$ using Eq. (2). For each nominal energy where angular distributions were taken, the effective reaction energies determined at each angle were then averaged to give E, the nominal center-of-mass energy.

For each energy the quantities $S_i\overline{W}^i_L(\varepsilon)$ were fitted using Eq. (7), with $P_\ell(\cos\theta_L)$ replaced by $Q^\varepsilon_\ell P_\ell(\cos\theta_D)$. The parameters S_i, a^i_1, a^i_2, and a^i_3 were varied; $a^i_{\ell>3}$ were set to zero. The fit was fully determined, since data were available at four independent angles. For each fit the needed Q^ε_ℓ were calculated once at the average γ-ray energy. The neglect of $\ell > 3$ terms in the angular distribution is justified on the grounds that the terms are very small due to the higher multipolarity and/or initial angular momentum required. Sample angular distributions obtained for $E = 417$ and $E = 848$ keV are shown in Fig. 8. The errors in the a^i_ℓ are dominated by statistics; the systematic error due to uncertainties in the detection efficiencies, detector angles, and attenuation coefficients is estimated to be ± 0.03.

Substantial target deterioration took place during the $E = 116$ keV angular-distribution measurement. Due to the large uncertainty from this deterioration, these data were analyzed by normalizing the γ_0 and γ_1 yields to the γ_2 yield. The γ_2 angular distribution was assumed to be isotropic in center of mass (which was observed to be satisfied for the measurements at other energies).

2. 0° data

As above, the factors $\overline{W}^i_L(\delta)$ used in Eqs. (9)–(12) were calculated by taking a^0_2 and a^1_2 from Ref. [39], setting $a^0_1 = 0.0$, $a^0_3 = 0.05$, $a^1_1 = 0.08$, $a^1_3 = -0.05$, and setting $a^i_{\ell>3}$ to zero. These choices will be justified by the results presented in Sec. IV. The cross sections $\sigma_i(E)$ were then extracted using Eq. (13), and converted to $S_i(E)$ using Eq. (2).

3. All data

Since S_1 must equal S_2, the ratio S_1/S_2 was compared to unity in order to test internal consistency; the results were consistent with unity within an accuracy of 4%. The weighted average of S_1 and S_2 (using statistical errors) was taken to form S_{12}. Then S_0 and S_{12} were added together to give S, the total S factor. The error explicitly included with S results from errors due to statistics, ΔF_L, Δf, and uncertainty in the center-of-mass energy (from the Q value, γ-ray energy calibration, statistical error in centroid, and attenuation coefficients), combined in quadrature. Additional systematic uncertainties are listed in Table II.

The branching ratio R is calculated by dividing the weighted average of γ_1 and γ_2 by γ_0: $R = S_{12}/S_0$. The

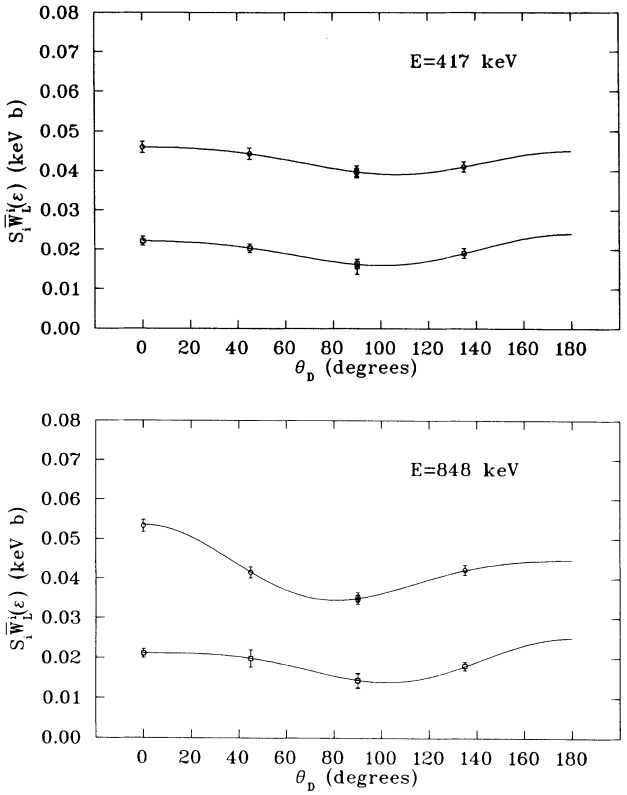

FIG. 8. The measured γ_0 (circles) and γ_1 (squares) yields with statistical errors are plotted as a function of detector angle for $E = 417$ and $E = 848$ keV. The solid curves are the fits to Eq. (7) described in the text.

TABLE II. Systematic errors in the absolute cross section. The total is computed by adding the individual errors in quadrature.

Source of Error	Error (%)	
^{3}H areal density		
^{3}H(d,α) cross section	3	
Detector solid angle	1.5	
Current integration	2	
Statistics	0.8	
Uniformity	1	
	4.1	4.1
γ-ray detection efficiency		3
Current integration		1
Angular-distribution correction		3
Total		6

error explicitly included with R is statistical; the systematic error in R is estimated to be 4%.

IV. RESULTS

A. Total S factor

The total S factors obtained with the different targets and in different geometries are shown in Fig. 9. The data taken under different experimental conditions are seen to be in excellent agreement. It is also seen that the energy dependence of the data is well described by the theoretical results of Kajino, Toki, and Austin [38]. We adopt this energy dependence as a means of comparing and combining the different data sets. The results for fits to this energy dependence are shown in Table III. The data sets were combined by first slightly renormalizing each set so that the fitted $S(0) = 0.1067$ keV b, and then taking the weighted average of S and E for data points whose energies were within $\lesssim 10$ keV. The weighted averages for the branching ratio R (presented below) were also formed using statistical errors and the same energy binning used for S. The systematic uncertainty in S due to the Q value was not included in making the weighted average, but was included after doing so; this uncertainty amounts to 6% for the lowest-energy S measurement. The final results for S are shown in Fig. 10. The error bars do not include an additional systematic error of 6% (Table II); of the total systematic error, the energy-dependent contributions due to γ-ray efficiency and angular-distribution corrections are estimated to be $\lesssim 4\%$.

TABLE III. The resulting $S(0)$ values found from fits of the energy dependence of Ref. [38] to data taken under different experimental conditions. Also given are the number of data points N and the χ^2 for each fit. The numbers in parentheses are the statistical errors in the least significant digits.

Data set	N	$S(0)$ (keV b)	χ^2
Target 1, geom. A	19	0.1060(6)	23.0
Target 1, geom. B	2	0.1067(18)	0.008
Target 3, geom. A	8	0.1074(9)	7.96
Target 3, geom. B	2	0.1049(21)	2.44
Target 4, geom. C	9	0.1053(8)	5.33
Target 5, geom. A	8	0.1109(12)	4.17
Target 5, geom. B	1	0.1116(33)	0.0
All data	49	0.1067(4)	64.3

B. Branching ratio

The results for the branching ratio R are shown in Fig. 10, and are consistent with a constant; a fit of the 17 data points to a constant using statistical errors yields $R = 0.453(2)$, with $\chi^2 = 40.1$. A fit to a lin-

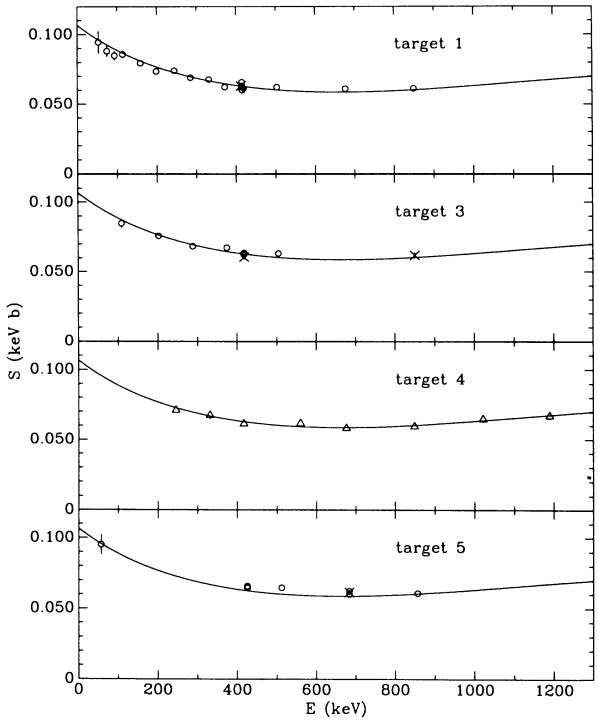

FIG. 9. Total S factors obtained from targets 1 and 3–5. The circles, crosses, and triangles correspond to data taken in geometries A, B, and C, respectively. The solid curves are the theoretical results of Ref. [38], normalized to $S(0) = 0.1067$ keV b.

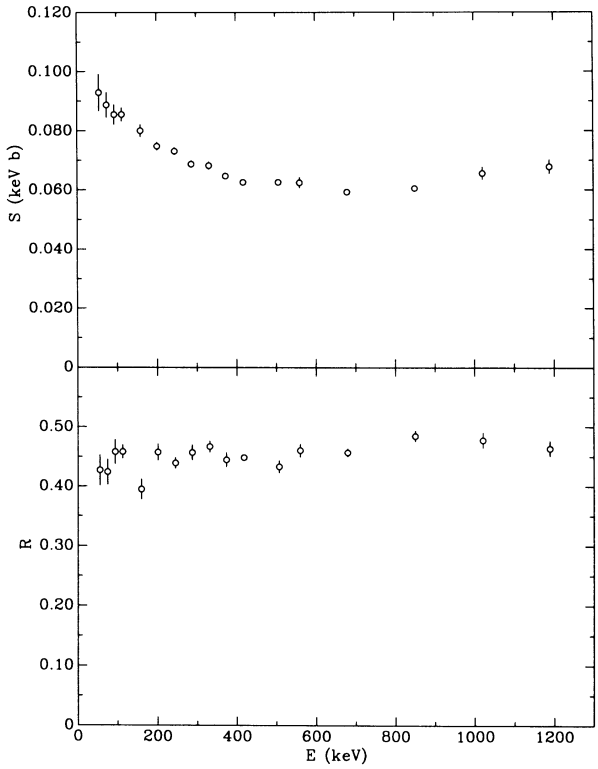

FIG. 10. Upper panel: The final results for S, found by combining the data sets shown in Fig. 9. The error bars do not include the additional systematic error of 6%. Lower panel: The branching ratio R; the systematic error is estimated to be 4%.

ear dependence yields an improved fit: $R(0) = 0.437(5)$, $dR/dE = 3.4(9) \times 10^{-5}$ keV^{-1}, with $\chi^2 = 27.1$, but this energy dependence is within the estimated 4% systematic error.

C. Angular distributions

The measured Legendre coefficients for the γ_0 and γ_1 transitions are shown in Fig. 11. The results for γ_1 are similar to γ_0, except that the errors are significantly larger due to poorer statistics. The results for a_2^i are seen to be in reasonable agreement with the calculation of Tombrello and Parker [39]. Comparisons of the a_2^i coefficients to the Tombrello-Parker calculation as well as fits to a constant for a_1^i and a_3^i are described in Table IV. The Tombrello-Parker calculation and the values obtained from fits to a constant for the odd terms have been adopted for the analysis of the zero-degree data. The constant fits were chosen for simplicity; the Legendre coefficients are expected to be slowly varying functions of energy, but the limited statistics mask any energy dependence. The values adopted have little impact on the final results: setting $a_1^i = a_3^i = 0$ changes the extracted values of S and R by $\approx$ 1–2 %.

V. DISCUSSION

A. Comparison with previous experiments

Our results for S are consistent with the previous direct measurements for $E \gtrsim 200$ keV, if systematic errors are taken into consideration. However, for $E \lesssim 150$ keV, the present data are $\approx 40\%$ lower than the data of Schröder *et al.* [8] (the only previous experiment in this range). For $E \gtrsim 250$ keV, our results for S are consistent with the Coulomb-breakup results of Utsunomiya *et al.* [12], but are considerably lower at lower energies. The agreement with the Coulomb-breakup data at higher energies is not surprising since their results are normalized to $S(500\text{ keV}) = 0.060$ keV b. The 6% systematic error in the present experiment is considerably smaller than the 14–25 % systematic errors in the previous experiments.

The present results for the branching ratio R are consistent with the data of Griffiths *et al.* [7] and Burzynski *et al.* [9], but are about 40% higher than those of Schröder *et al.* The statistical and systematic errors are considerably reduced compared to the previous experiments.

Our measurements of the angular distributions are consistent with the limited measurements of Griffiths *et al.* at $E = 241$ and 567 keV.

B. Comparison with theoretical calculations

The present data are compared in Fig. 12 to the theoretical energy dependences of Kajino, Toki, and Austin [38], Langanke [16], Mertelmeier and Hofmann [17], Altmeyer *et al.* [using their Modified Hasegawa-Nagata (MHN) interaction calculation] [18], and Mohr *et al.* [19]. The calculated energy dependences are seen to be consistent with each other, within about 10%. The data are consistent with all of the energy dependences, except perhaps that of Mertelmeier and Hofmann [17].

Calculations of the energy dependence at very low energies show some disagreement. Using a direct capture model, Williams and Koonin [40] calculated an expansion for the low-energy logarithmic derivative,

$$\frac{1}{S}\frac{dS}{dE} = a + bE\,, \tag{16}$$

with $a = -2.034$ MeV^{-1} and $b = -3.709$ MeV^{-2}. Kajino [41] has argued that the Williams-Koonin calculation contains a computational error; he finds $a = -1.15$ MeV^{-1} with what appears to be an identical calculation. The negative sign of b is inconsistent with the

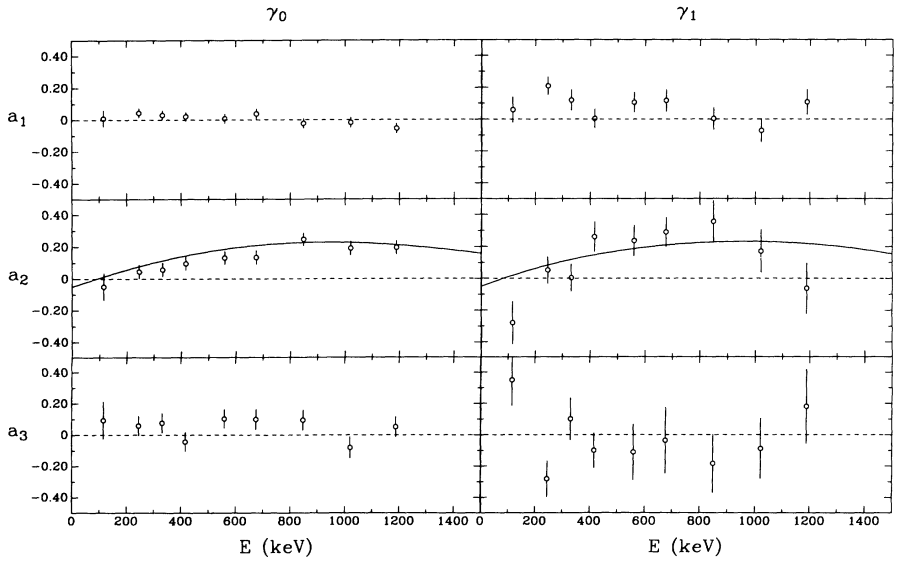

FIG. 11. γ_0 and γ_1 angular-distribution coefficients. The errors are statistical; the systematic uncertainty in a_ℓ is estimated to be ± 0.03. The solid curves are the calculations of Tombrello and Parker [39] for a_2.

TABLE IV. Fits of the γ_0 and γ_1 Legendre coefficients (nine data points for each coefficient) to either a constant or the Tombrello-Parker [39] calculation. In the case of the Tombrello-Parker calculation, there are no variable parameters. The parametrization used in the analysis of the zero-degree data is listed in the column under "Adopted." The numbers in parentheses are the statistical errors in the least significant digits.

Coefficient	Function	Result	χ^2	Adopted
a_1^0	constant	0.007 (10)	8.9	0.0
a_2^0	Ref. [39]		9.3	Ref. [39]
a_3^0	constant	0.05(2)	8.2	0.05
a_1^1	constant	0.08(2)	13.2	0.08
a_2^1	Ref. [39]		13.6	Ref. [39]
a_3^1	constant	−0.05(5)	12.9	−0.05

positive curvature found in all other calculations. Values of a from other calculations (-2.056 MeV^{-1} [38], -2.0 MeV^{-1} [42], -1.02 MeV^{-1} [19]) vary by a factor of 2, even though the overall agreement of the energy dependences is within $\approx 10\%$ (Fig. 12).

The calculations of the absolute magnitude of the S factor show considerable dispersion. Resonating-group method (RGM) calculations [14,15,17,18,43] find considerable dependence upon the effective interaction used. Although Chopovsky [43] finds $S(0) = 0.154$ keV b, most calculations favor $S(0) \approx 0.10$–0.11, using the interaction which best reproduces the ^{7}Li bound state properties and also the mirror $^3\mathrm{He}(\alpha,\gamma)^7\mathrm{Be}$ reaction. Calculations using other techniques show similar dispersion. Langanke [16] has found $S(0) \approx 0.105$ keV b using a microscopic potential model. Kajino, Bertsch, and Kubo [44] have estimated $S(0) = 0.097 \pm 0.038$ keV b using the measured electric-dipole polarizability of ^{7}Li. Kajino *et al.* [45] have found a constraint on $S(0)$, $0.083 \leq S(0) \leq 0.15$ keV b, using the experimental matter radius of ^{7}Li, and the correlation found in RGM calculations between $S(0)$ and the matter radius. Potential-model calculations of $S(0) = 0.09 \pm 0.03$ keV b and $S(0) = 0.100$ keV b have been reported by Buck and Merchant [42] and Mohr *et al.* [19], respectively.

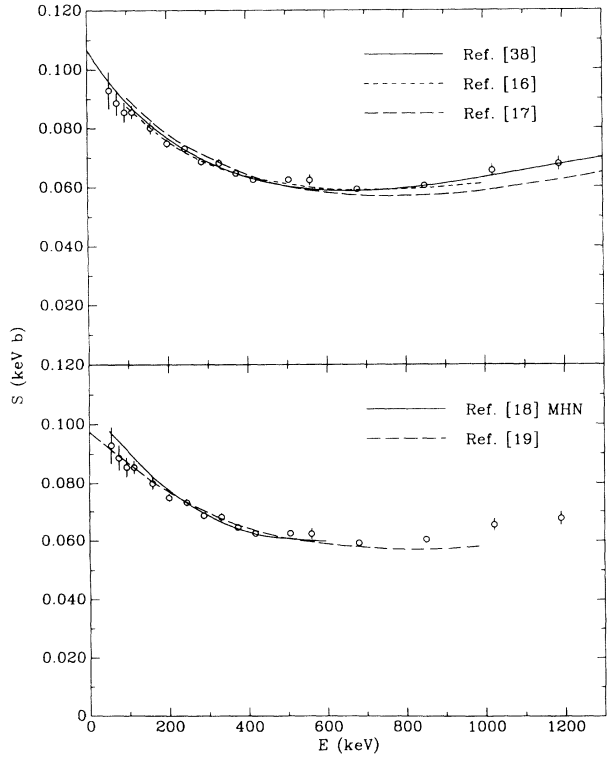

FIG. 12. Comparison of various theoretical calculations of $S(E)$, normalized for best fit to the data.

The branching ratios found in the present experiment are consistent with all calculations [15,18–20], which predict R in the range 0.41–0.47. The strong theoretical objections [18,20] to the branching ratio reported by Schröder *et al.* have proven to be well founded.

As discussed in Sec. IV C, the measured a_2^i coefficients are consistent with the calculations of Tombrello and Parker. There are no theoretical calculations of the a_1^i and a_3^i coefficients, but the results are consistent with the expectation that a_1^i and a_3^i would be less significant than a_2^i, due to relative weakness of the interfering $M1$ or $E2$ amplitudes.

VI. THERMONUCLEAR REACTION RATE

For the calculation of the thermonuclear reaction rate, we assumed $S(E)$ to be given for $E \leq 1200$ keV by the energy dependence of Ref. [38] with $S(0) = 0.1067$ keV b (i.e., normalized to our data), and for higher energies by a linear extrapolation:

$$S(E) = 0.0337 + 2.85 \times 10^{-5} E \ (\mathrm{keV\ b}) \qquad (E > 1200 \ \mathrm{keV}) \quad (17)$$

where E is in keV. Using this parametrization, the reaction rate $N_A\langle\sigma v\rangle$ was then calculated by numerically integrating Eq. (1). Energies between 50 and 1200 keV (i.e., the range covered by this experiment) contribute at least 50% of the integral in Eq. (1) for $0.09 \leq T_9 \leq 6$. The present reaction rate is in excellent agreement with that given by Caughlan and Fowler [46] for $T_9 \leq 1$, but is considerably lower for higher temperatures. Our numerically integrated reaction rate is given within $\approx 1\%$ for $T_9 \leq 10$ by the following expression (plotted in Fig. 13):

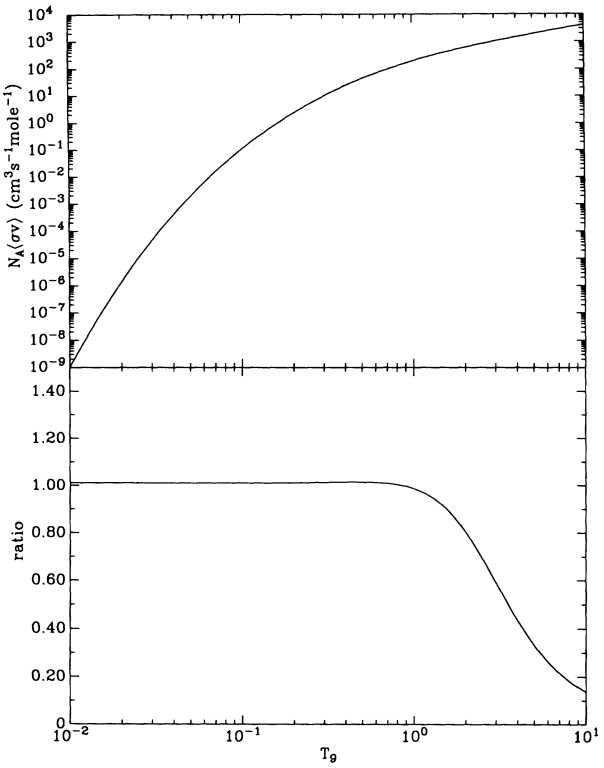

FIG. 13. The thermonuclear reaction rate $N_A\langle\sigma v\rangle$ calculated from our data is shown as a function of temperature in GK in the upper panel. The ratio of the present reaction rate to that given by Caughlan and Fowler [46] is shown in the lower panel.

$$N_A\langle\sigma v\rangle = 8.79\times10^5 T_9^{-2/3}\exp\left(-\frac{8.080}{T_9^{1/3}}\right) \times(1+0.0516T_9^{1/3}-0.711T_9^{2/3} +0.367T_9-0.00581T_9^2). \quad (18)$$

VII. CONCLUSIONS

We have measured the ^{3}H(α,γ)^{7}Li cross section for $50 \le E \le 1200$ keV, with a systematic uncertainty estimated to be 6%. Nine angular distributions were measured between 115 and 1200 keV. The present results disagree at low energies ($E \lesssim 200$ keV) with the two previous experiments [8,12], which show a larger increase in the low-energy S factor than predicted by theoretical calculations of the energy dependence. Our measurements of the branching ratio (we find $R \approx 0.45$) are in reasonable agreement with Griffiths *et al.* [7] and Burzynski *et al.* [9], but not with Schröder *et al.* [8] (who found $R = 0.32 \pm 0.01$). The systematic error in the present experiment is reduced by a factor of 2–4 compared to the previous measurements, leading to a much better determination of the absolute normalization of the cross section. The energy dependence of the cross section, the magnitude of the branching ratio, and the angular distributions are in reasonable agreement with the available calculations.

While the data are in reasonable agreement with the theoretical calculations of the energy dependence [15–19], it would be useful if the existing $\sim$ 10% discrepancies (see Fig. 12) between the calculations could be resolved. However, it may be that this uncertainty represents the best that can be achieved with current theoretical techniques. An improved understanding of the energy dependence would reduce the uncertainty in the cross section at low energies, where the data have larger uncertainties, or are unavailable. However, it is important to note that the present experiment covers nearly all of the energy range needed for standard big-bang nucleosynthesis, so astrophysical conclusions do not depend very much on the extrapolation of data. It would also be interesting to perform another ^{7}Li Coulomb-breakup experiment, under improved kinematical conditions, in order to test the accuracy of radiative-capture cross sections determined in this approach.

Our new reaction rate does not differ significantly from the Caughlan-Fowler compilation in the temperature range needed for standard big-bang nucleosynthesis. The error in the ^{3}H(α,γ)^{7}Li reaction rate is now comparable to other nuclear-physics uncertainties, reducing a major source of uncertainty in the comparison of big-bang calculations with the observed light-element abundances.

ACKNOWLEDGMENTS

The authors thank R. E. Azuma for providing the titanium-tritide targets used in the preliminary phase of this experiment. This work was supported in part by the National Science Foundation, Grant No. PHY91-15574.

[1] L. M. Krauss and P. Romanelli, Astrophys. J. **358**, 47 (1990).
[2] S. P. Riley and J. M. Irvine, J. Phys. G **17**, 35 (1991).
[3] T. P. Walker, G. Steigman, D. N. Schramm, K. A. Olive, and H.-S. Kang, Astrophys. J. **376**, 51 (1991).
[4] M. S. Smith, L. H. Kawano, and R. A. Malaney, Astrophys. J., Suppl. Ser. **85**, 219 (1993).
[5] A. H. Wapstra (private communication).
[6] C. R. Brune, Ph.D. thesis, California Institute of Technology, 1994.
[7] G. M. Griffiths, R. A. Morrow, P. J. Riley, and J. B. Warren, Can. J. Phys **39**, 1307 (1961).
[8] U. Schröder, A. Redder, C. Rolfs, R. E. Azuma, L. Buchmann, C. Campbell, J. D. King, and T. R. Donoghue, Phys. Lett. B **192**, 55 (1987).
[9] S. Burzynski, K. Czerski, A. Marcinkowski, and

P. Zupranski, Nucl. Phys. **A473**, 179 (1987).
[10] G. Feldman, M. J. Balbes, L. H. Kramer, J. Z. Williams, H. R. Weller, and D. R. Tilley, Phys. Rev. C **42**, R1167 (1990).
[11] J. E. Perry, Jr., and S. J. Bame, Jr., Phys. Rev. **99**, 1368 (1955).
[12] H. Utsunomiya, Y.-W. Lui, D. R. Haenni, H. Dejbakhsh, L. Cooke, B. K. Srivastava, W. Turmel, D. O'Kelly, R. P. Schmitt, D. Shapira, J. Gomez del Campo, A. Ray, and T. Udagawa, Phys. Rev. Lett. **65**, 847 (1990); **69**, 863(E) (1992).
[13] S. B. Gazes, J. E. Mason, R. B. Roberts, and S. G. Teichmann, Phys. Rev. Lett **68**, 150 (1992).
[14] T. Kajino and A. Arima, Phys. Rev. Lett. **52**, 739 (1984).
[15] T. Kajino, Nucl. Phys. **A460**, 559 (1986).
[16] K. Langanke, Nucl. Phys. **A457**, 351 (1986).
[17] T. Mertelmeier and H. M. Hofmann, Nucl. Phys **A459**, 387 (1986).
[18] T. Altmeyer, E. Kolbe, T. Warmann, K. Langanke, and H. J. Assenbaum, Z. Phys. A **330**, 277 (1988).
[19] P. Mohr, H. Abele, R. Zwiebel, G. Staudt, H. Krauss, H. Oberhummer, A. Denker, J. W. Hammer, and G. Wolf, Phys. Rev. C **48**, 1420 (1993)
[20] T. Kajino, G. J. Mathews, and K. Ikeda, Phys. Rev. C **40**, 525 (1989).
[21] F. Ajzenberg-Selove, Nucl. Phys. **A475**, 1 (1987).
[22] P. M. Endt, Nucl. Phys. **A521**, 1 (1990).
[23] T. R. Wang, R. B. Vogelaar, and R. W. Kavanagh, Phys. Rev. C **43**, 883 (1991); **44**, 1226(E) (1991).
[24] J. W. Maas, A. J. C. D. Holvast, A. Baghus, H. J. M. Aarts, and P. M. Endt, Nucl. Phys. **A301**, 213 (1978).
[25] C. R. Brune and R. W. Kavanagh, Nucl. Instrum. Methods Phys. Res. Sect. A **343**, 415 (1994).
[26] V. Ya. Golovnya, A. P. Klyucharev, B. A. Shilyaev, and N. A. Shlyakhov, Yad. Fiz. **4**, 770 (1967) [Sov. J. Nucl. Phys. **4**, 547 (1967)].
[27] J. F. Ziegler, *The Stopping and Ranges of Ions In Matter* (Pergamon, New York, 1977), Vols. 3 and 4.
[28] D. G. Sargood, Phys. Rep. **93**, 61 (1982).
[29] M. Drosg and O. Schwerer, *Handbook on Nuclear Activation Data* (International Atomic Energy Agency, Vienna, 1987), p. 83.
[30] R. C. Greenwood, R. G. Helmer, and R. J. Gehrke, Nucl. Instrum. Methods **159**, 465 (1979).
[31] C. R. Brune, I. Licot, and R. W. Kavanagh, Phys. Rev. C **48**, 3119, (1993).
[32] F. Ajzenberg-Selove, Nucl. Phys. **A490**, 1 (1988).
[33] P. Paul, J. B. Thomas, and S. S. Hanna, Phys. Rev. **147**, 774 (1966).
[34] W. R. Nelson, H. Hirayama, and D. W. O. Rodgers, SLAC Report No. 265, 1985.
[35] M. E. Rose, Phys. Rev. **91**, 610 (1953).
[36] T. M. Semkow, G. Mehmood, P. P. Parekh, and M. Virgil, Nucl. Instrum. Methods Phys. Res. Sect. A **290**, 437 (1990).
[37] H. F. Winters, in *Radiation Effects on Solid Surfaces*, edited by M. Kaminsky (American Chemical Society, Washington, DC, 1976), pp. 1–29.
[38] T. Kajino, H. Toki, and S. M. Austin, Astrophys. J. **319**, 531 (1987); **327**, 1060(E) (1988).
[39] T. A. Tombrello and P. D. Parker, Phys. Rev. **131**, 2582 (1963).
[40] R. D. Williams and S. E. Koonin, Phys. Rev. C **23**, 2773 (1981).
[41] T. Kajino, in *Origin and Distribution of the Elements*, edited by G. J. Mathews (World Scientific, Singapore, 1988), pp. 700–714.
[42] B. Buck and A. C. Merchant, J. Phys. G **14**, L211 (1988).
[43] L. L. Chopovsky, Phys. Lett. B **229**, 316 (1989).
[44] T. Kajino, G. F. Bertsch, and K.-I. Kubo, Phys. Rev. C **37**, 512 (1988).
[45] T. Kajino, H. Toki, K.-I. Kubo, and I. Tanihata, Phys. Lett. B **202**, 475 (1988).
[46] G. R. Caughlan and W. A. Fowler, At. Data Nucl. Data Tables **40**, 283 (1988).